

Third-order intrinsic alignment of SDSS BOSS LOWZ galaxies

Laila Linke^{1,2*}, Susan Pyne³, Benjamin Joachimi³, Christos Georgiou⁴, Kai Hoffmann⁵, Rachel Mandelbaum⁶, Sukhdeep Singh⁶

¹ Universität Innsbruck, Institut für Astro- und Teilchenphysik, Technikerstr. 25/8, 6020 Innsbruck, Austria

² Universität Bonn, Argelander-Institut für Astronomie, Auf dem Hügel 71, 53121 Bonn, Germany

³ Department of Physics and Astronomy, University College London, Gower Street, London WC1E 6BT, UK

⁴ Institute for Theoretical Physics, Utrecht University, Princetonplein 5, 3584 CC, Utrecht, The Netherlands.

⁵ Institute of Space Sciences (ICE, CSIC), Campus UAB, Carrer de Can Magrans, s/n, 08193 Barcelona, Spain

⁶ McWilliams Center for Cosmology & Astrophysics, Department of Physics, Carnegie Mellon University, Pittsburgh, PA 15213, USA

June 10, 2024

ABSTRACT

Cosmic shear is a powerful probe of cosmology, but it is affected by the intrinsic alignment (IA) of galaxy shapes with the large-scale structure. Upcoming surveys like *Euclid* and Vera C. Rubin Observatory's Legacy Survey of Space and Time (LSST) require an accurate understanding of IA, particularly for higher-order cosmic shear statistics that are vital for extracting the most cosmological information. In this paper, we report the first detection of third-order IA correlations using the LOWZ galaxy sample from the Sloan Digital Sky Survey (SDSS) Baryon Oscillation Spectroscopic Survey (BOSS). We compare our measurements with predictions from the MICE cosmological simulation and an analytical NLA-inspired model informed by second-order correlations. We also explore the dependence of the third-order correlation on the galaxies' luminosity. We find that the amplitude A_{IA} of the IA signal is non-zero at the 4.7σ (7.6σ) level for scales between $6 h^{-1}$ Mpc ($1 h^{-1}$ Mpc) and $20 h^{-1}$ Mpc. For scales above $6 h^{-1}$ Mpc the inferred A_{IA} agrees both with the prediction from the simulation and estimates from second-order statistics within 1σ but deviations arise at smaller scales. Our results demonstrate the feasibility of measuring third-order IA correlations and using them for constraining IA models. The agreement between second- and third-order IA constraints also opens the opportunity for a consistent joint analysis and IA self-calibration, promising tighter parameter constraints for upcoming cosmological surveys.

Key words. large-scale structure of Universe, Gravitational lensing: weak, cosmology: observations

1. Introduction

Cosmic shear, the correlations between galaxy shapes due to the weak gravitational lensing by the cosmic large-scale structure, is a popular and constraining probe of cosmology. Cosmic shear surveys such as the Dark Energy Survey (DES, Abbott et al. 2016; Becker et al. 2016), the Kilo-Degree Survey (KiDS, Kuijken et al. 2015), or the Hyper-Suprime-Cam survey (HSC, Aihara et al. 2018) have constrained the parameter $S_8 = \sigma_8 \sqrt{\Omega_m/0.3}$, a combination of the matter density parameter Ω_m and the clustering parameter σ_8 , at 2–4 per cent (Asgari et al. 2021; Amon et al. 2022; Dalal et al. 2023; Li et al. 2023). Soon, even more extensive and deeper surveys like *Euclid* (Laureijs et al. 2011; *Euclid* Collaboration: Mellier et al. 2024), Vera C. Rubin Observatory's Legacy Survey of Space and Time (LSST, Ivezić et al. 2019) or the Nancy Grace Roman space telescope (Akeson et al. 2019) will use cosmic shear to not only better constrain Ω_m and σ_8 , but also determine the time evolution of dark energy and the mass of neutrinos. Arguably, cosmic shear is now entering its most exciting phase as a probe of our Universe.

While the increasing size of the data sets provides more and more precision, the accuracy of theoretical predictions also needs to be updated. For this, several astrophysical effects that impact cosmic shear measurements must be understood. One such effect is the alignment between the intrinsic shapes of galaxies, the so-called intrinsic alignment (IA, Lamman et al. 2024; Troxel & Ishak 2015; Joachimi et al. 2015). IA occurs due

to the formation of galaxies within the dark matter-dominated gravitational field (Catelan et al. 2001). Elliptical galaxies tend to be aligned with the gravitational tidal field, leading to a radial alignment with respect to matter overdensities (Kiessling et al. 2015). These alignments add to the observed shape correlations and thus contaminate the cosmic shear signal.

If IA is not taken into account in cosmic shear analyses, inferred parameters can be severely biased (Hirata et al. 2007; Kirk et al. 2015). Therefore, cosmic shear analyses commonly incorporate a description for IA in their model with some free parameters that are constrained in the inference simultaneously with the cosmological parameters.

Several IA models have been proposed for this purpose. A relatively simple model is the non-linear linear alignment (NLA) model by Bridle & King (2007). This empirical model assumes that the power spectrum of galaxy shapes is linearly related to the non-linear matter power spectrum via a free parameter A_{IA} describing the amplitude of the correlation. While it is only a phenomenological description, it fits IA measurements well. There are also other more physically motivated models, such as the Tidal Alignment and Tidal Torque (TATT) model (Blazek et al. 2019), which allows galaxies to not align solely with the gravitational tidal field but also the tidal torque and includes a density weighting term. Alternatively, there are halo model descriptions (Schneider & Bridle 2010; Fortuna et al. 2021), which explicitly distinguish between central and satellite galaxies inside dark matter halos. Other models are based on perturbative approaches (Vlah et al. 2020; Maion et al. 2023; Chen & Kokron 2024). It is

* Corresponding author, e-mail: laila.linke@uibk.ac.at

unclear which IA model is the most appropriate for any specific analysis.

However, the choice of model can impact cosmological parameter constraints. *DES and KiDS Collaboration: Abbott et al. (2023)* found in a combined analysis of DES and KiDS that using the TATT instead of the NLA model can lower the inferred value for S_8 by almost 3 per cent, corresponding to a shift by 0.9σ . Consequently, it is paramount to test IA models independently of cosmic shear measurements to find an appropriate model. Furthermore, independent constraints of IA model parameters can be used as priors for cosmic shear analyses, significantly tightening constraints on other parameters (*Johnston et al. 2019*).

IA studies so far have been mainly concerned with second-order correlations of matter overdensity and intrinsic galaxy shapes. Mostly the shape-shape and density-shape correlations were constrained (e.g. *Joachimi et al. 2011; Singh et al. 2015; Singh & Mandelbaum 2016; Johnston et al. 2019; Fortuna et al. 2021; Johnston et al. 2021; Samuroff et al. 2023*). For several reasons, though, it has become increasingly interesting to study higher-order statistics (HOS), for example third-order correlations. For example, while current IA models are well-designed to describe second-order IA correlations, it is an important consistency check to see whether they also match higher-order correlations. An example of such a test was carried out by *Pyne et al. (2022)*, who measured the IA power- and bispectrum in simulations and found that the same model parameters could describe both. Furthermore, HOS depend differently on both cosmological and IA parameters. Combining second-order and HOS can reduce parameter degeneracies and lead to better constraints (e.g. *Burger et al. 2024; Euclid Collaboration: Ajani et al. 2023*). Adding higher-order information can also help in self-calibrating systematic effects like IA (*Pyne & Joachimi 2021*). Analyses like these are vital to optimally use the data sets of *Euclid* and *LSST*, but they can only be performed if we can ensure we understand how systematic effects like IA behave for third-order statistics. As shown by *Semboloni et al. (2008)* using cosmological simulations, third-order correlations of intrinsic galaxy shapes and the matter field can significantly impact analysis of third-order cosmic shear and contribute as much as 15% of the signal for surveys with a median redshift of 0.7. Consequently, we must include IA in the modelling of the third-order cosmic shear signal and demonstrate that our models can accurately describe higher-order correlations of the matter overdensity and the intrinsic shapes of galaxies.

In this paper, we take the first step towards this by reporting the first detection of third-order intrinsic alignment correlations in the low-redshift (LOWZ) galaxy sample from the SDSS BOSS survey. This sample contains spectroscopically observed luminous red galaxies (LRGs) at redshifts below 0.4. For this sample, *Singh et al. (2015)* measured second-order correlations between the matter density and the shapes and between shapes of different galaxies. The measurement was conducted by using the positions of galaxies as tracers for the matter distribution and comparing them pairwise to the galaxies' shapes. We follow in their footsteps by comparing the positions of galaxy pairs with the shape of a third galaxy, thus measuring the density-density-shape correlation. This correlation is then compared to predictions by the MICE cosmological simulation and an analytical NLA-based model.

This paper is structured as follows. In Sect. 2, we define fundamental notations, describe the third-order intrinsic alignment correlation function and relate it to the matter-matter-shape bispectrum. In Sect. 3, we describe our estimator for the correlation function and our covariance estimate. Section 4 describes the

observed and simulated data sets. The measurements and comparisons to the analytical model are presented in Sect. 5. We conclude with a discussion in Sect. 6.

2. Theoretical background and modelling

2.1. Basic quantities and definitions

In the weak gravitational lensing limit (see e.g. *Bartelmann & Schneider 2001* for a review), the observed ellipticity $\epsilon(\boldsymbol{\theta})$ of a source galaxy at angular position $\boldsymbol{\theta}$ is determined by its intrinsic ellipticity $\epsilon_1(\boldsymbol{\theta})$ and the weak lensing shear $\gamma(\boldsymbol{\theta})$, both of which are complex quantities. In weak lensing, $|\gamma| \ll 1$, and,

$$\epsilon(\boldsymbol{\theta}) = \epsilon_1(\boldsymbol{\theta}) + \gamma(\boldsymbol{\theta}). \quad (1)$$

Under the flat sky approximation, the shear is related to the lensing convergence κ via the Kaiser-Squires relation (*Kaiser & Squires 1993*)

$$\tilde{\gamma}(\boldsymbol{\ell}) = e^{2i\phi_\ell} \tilde{\kappa}(\boldsymbol{\ell}), \quad (2)$$

where the tilde denotes Fourier transform and ϕ_ℓ is the polar angle of the angular frequency $\boldsymbol{\ell}$. Analogously, we can define an 'intrinsic alignment (IA) convergence' κ_1 , which describes the convergence that would cause a shear equivalent to the intrinsic source ellipticity via

$$\tilde{\epsilon}_1(\boldsymbol{\ell}) = e^{2i\phi_\ell} \tilde{\kappa}_1(\boldsymbol{\ell}). \quad (3)$$

For source galaxies distributed with a probability distribution $p(\chi)$ with comoving distance χ , $\kappa(\boldsymbol{\theta})$ is a weighted integral over the $\kappa(\boldsymbol{\theta}, \chi)$ at each χ ,

$$\begin{aligned} \kappa(\boldsymbol{\theta}) &= \int d\chi p(\chi) \kappa(\boldsymbol{\theta}, \chi) \\ &= \int d\chi p(\chi) \int d\chi' W(\chi, \chi') \delta(\chi' \boldsymbol{\theta}, \chi'), \end{aligned} \quad (4)$$

where we assumed a flat Universe, $\delta(\chi' \boldsymbol{\theta}, \chi)$ is the matter density contrast at angular position $\boldsymbol{\theta}$ and distance χ , and W is the lensing efficiency given by

$$W(\chi, \chi') = \frac{3 H_0^2 \Omega_m}{2c^2} \frac{\chi(\chi - \chi')}{\chi' a(\chi)}, \quad (5)$$

where H_0 is the Hubble constant, Ω_m is the matter density parameter, and $a(\chi)$ is the scale factor at co-moving distance χ . The κ_1 can be related to a density contrast δ_1 , which would cause a shear equivalent to the intrinsic galaxy ellipticity,

$$\kappa_1(\boldsymbol{\theta}) = \int d\chi p(\chi) \delta_1(\chi \boldsymbol{\theta}, \chi). \quad (6)$$

We are interested in correlations between the intrinsic ellipticity field δ_1 and the matter density contrast δ . To study these correlations, we use galaxy positions as tracers of the matter field. Their distribution is characterised by their three-dimensional number density $n(\chi \boldsymbol{\theta}, \chi)$ at angular position $\boldsymbol{\theta}$ and distance χ . This density is related to the galaxy number density contrast δ_g by

$$n(\chi \boldsymbol{\theta}, \chi) = \bar{n}(\chi) [\delta_g(\chi \boldsymbol{\theta}, \chi) + 1], \quad (7)$$

where $\bar{n}(\chi)$ is the average number density at comoving distance χ . From this, we also define the projected, two-dimensional galaxy number density $N(\boldsymbol{\theta})$ as

$$N(\boldsymbol{\theta}) = \int d\chi p(\chi) n(\chi \boldsymbol{\theta}, \chi), \quad (8)$$

whose average we denote as \bar{N} .

2.2. Intrinsic alignment correlation functions

Since the intrinsic ellipticity of an individual galaxy is unknown, its observed ellipticity alone does not contain usable cosmological information. Instead, one needs to consider the correlation functions of the ellipticities. The most commonly used ones are the second-order correlations, either of the ellipticities ϵ with themselves (i.e. ‘cosmic shear’) or between ellipticities and the galaxy number density N (i.e. ‘galaxy-galaxy-lensing’). Here, though, we are interested in third-order correlation functions. For this, we have, in principle, three choices: correlating the ellipticities at three different positions (‘third-order cosmic shear’, [Schneider & Lombardi 2003](#)), the ellipticities at two positions with the galaxy number density at a third position, or the ellipticity at one position with the number density at two different positions (‘galaxy-galaxy-galaxy lensing’, G3L, [Schneider & Watts 2005](#)). The last of these, so-called shape-lens-lens G3L, has the highest signal-to-noise ratio ([Simon et al. 2012](#)), so we concentrate on this.

In general, the correlation function for G3L is

$$G'(\boldsymbol{\theta}_1, \boldsymbol{\theta}_2) = \frac{1}{\bar{N}^2} \left\langle N(\boldsymbol{\theta} + \boldsymbol{\theta}_1) N(\boldsymbol{\theta} + \boldsymbol{\theta}_2) \epsilon(\boldsymbol{\theta}) e^{-i(\phi_1 + \phi_2)} \right\rangle, \quad (9)$$

where the $\boldsymbol{\theta}_i$ are the angular separations between the lens galaxies and the shape tracing galaxy, with polar angles ϕ_i . This function can be decomposed into the sum of the contribution $G'_{\text{gg}\gamma}$ from the shear and G'_{ggI} from the intrinsic ellipticities as

$$G'_{\text{gg}\gamma}(\boldsymbol{\theta}_1, \boldsymbol{\theta}_2) = \frac{1}{\bar{N}^2} \left\langle N(\boldsymbol{\theta} + \boldsymbol{\theta}_1) N(\boldsymbol{\theta} + \boldsymbol{\theta}_2) \gamma(\boldsymbol{\theta}) e^{-i(\phi_1 + \phi_2)} \right\rangle, \quad (10)$$

and

$$G'_{\text{ggI}}(\boldsymbol{\theta}_1, \boldsymbol{\theta}_2) = \frac{1}{\bar{N}^2} \left\langle N(\boldsymbol{\theta} + \boldsymbol{\theta}_1) N(\boldsymbol{\theta} + \boldsymbol{\theta}_2) \epsilon_1(\boldsymbol{\theta}) e^{-i(\phi_1 + \phi_2)} \right\rangle. \quad (11)$$

If the distances χ of the considered lens and source galaxies are known, one can also measure the correlation functions G , $G_{\text{gg}\gamma}$, and G_{ggI} in terms of the projected physical separations between the galaxies, for example,

$$G_{\text{ggI}}(\mathbf{r}_1, \mathbf{r}_2) = \frac{1}{\bar{N}} \int d\chi p(\chi) \int d\chi_1 p(\chi_1) \int d\chi_2 p(\chi_2) \quad (12) \\ \times \left\langle n(\mathbf{r} + \mathbf{r}_1, \chi_1) n(\mathbf{r} + \mathbf{r}_2, \chi_2) \epsilon_1(\mathbf{r}, \chi) e^{-i(\phi_1 + \phi_2)} \right\rangle,$$

where $\epsilon_1(\mathbf{r}, \chi)$ is the intrinsic shape of a galaxy at projected galaxy separation \mathbf{r} on the sky (in physical units) and distance χ . The functions G and $G_{\text{gg}\gamma}$ can be defined analogously by replacing the intrinsic shape with the total observed shape or the shear.

Usually, when measuring the G3L correlation function, one uses lens and source samples that are well separated along the line of sight ([Simon et al. 2012](#); [Linke et al. 2020a](#)). This increases $G_{\text{gg}\gamma}$ since it depends on the correlation between the matter structures in front of the sources and the lens number density, weighted by the lensing efficiency W . This efficiency is stronger if the sources are farther away from the lensing structures and, thus, also the lens galaxies. The intrinsic contribution G_{ggI} , though, is down-weighted if lenses and sources are far apart from each other. This is because the intrinsic ellipticity of the sources depends primarily on their local density distribution. Therefore, the correlation to the lens number density is strongest if sources and lenses are at the same comoving distance. Here, we are particularly interested in G_{ggI} , so we reverse the usual

process of using well-separated lens and source samples. Instead, we explicitly measure the G3L signal only for lenses and sources with distances smaller than fixed physical distance Π_m . Thus, using Eq. (8), the correlation function we measure is

$$G^{\Pi_m}(\mathbf{r}_1, \mathbf{r}_2) \\ = \frac{1}{\bar{N}_{\Pi_m}^2} \int d\chi p(\chi) \int_{\chi - \Pi_m}^{\chi + \Pi_m} d\chi_1 p(\chi_1) \int_{\chi - \Pi_m}^{\chi + \Pi_m} d\chi_2 p(\chi_2) \quad (13) \\ \times \left\langle n(\mathbf{r} + \mathbf{r}_1, \chi_1) n(\mathbf{r} + \mathbf{r}_2, \chi_2) \epsilon(\mathbf{r}, \chi) e^{-i(\phi_1 + \phi_2)} \right\rangle,$$

where $\bar{N}_{\Pi_m}^2$ is the average number density of galaxy pairs within $\pm\Pi_m$,

$$\bar{N}_{\Pi_m}^2 = \int d\chi p(\chi) \left[\int_{\chi - \Pi_m}^{\chi + \Pi_m} d\chi_1 p(\chi_1) \bar{N}(\chi_1) \right]^2. \quad (14)$$

In principle, one can model G^{Π_m} for any Π_m by including both the IA and the cosmic shear contribution, as done for second-order statistics ([Samuroff et al. 2023](#)). Here, though, we choose a small Π_m such that the cosmic shear contribution is suppressed. This is possible because for a small enough Π_m , χ_1 and χ_2 are close to χ , so the lensing efficiency suppresses the correlation between n and the shear γ . Therefore, we can replace ϵ by the intrinsic shape ϵ_1 . Simultaneously, we choose Π_m large enough that all intrinsic alignment contributions to the correlation function are taken into account. Then, we can replace Π_m with infinity, so $G^{\Pi_m} \rightarrow G_{\text{ggI}}$. We test whether this assumption holds in Sect. 5 using the simulated data (see Sect. 4), which only includes IA and no cosmic shear contribution.

2.3. Aperture statistics

In the following, we are not directly analysing the correlation function but instead convert it to aperture statistics ([Schneider et al. 2002](#)). These have several practical advantages. For example, they can compress the data vector length from several hundred for the correlation function to a few tens. Moreover, they are more easily modelled from a bispectrum model than the correlation functions.

Aperture statistics are moments of aperture masses M'_{ap} ,

$$M'_{\text{ap}}(\theta; \boldsymbol{\theta}) = \int d^2\boldsymbol{\theta}' U_{\theta}(|\boldsymbol{\theta} - \boldsymbol{\theta}'|) \kappa(\boldsymbol{\theta}') \quad (15)$$

and aperture number counts N'_{ap} ,

$$N'_{\text{ap}}(\theta; \boldsymbol{\theta}) = \frac{1}{\bar{N}} \int d^2\boldsymbol{\theta}' U_{\theta}(|\boldsymbol{\theta} - \boldsymbol{\theta}'|) N(\boldsymbol{\theta}'), \quad (16)$$

where U_{θ} is a compensated filter function U_{θ} of aperture scale radius θ , that is $\int d\boldsymbol{\theta}' \boldsymbol{\theta}' U_{\theta}(\boldsymbol{\theta}') = 0$. The M'_{ap} can be linked to the shear via

$$M'_{\text{ap}}(\theta; \boldsymbol{\theta}) = \int d^2\boldsymbol{\theta}' Q_{\theta}(|\boldsymbol{\theta} - \boldsymbol{\theta}'|) \gamma(\boldsymbol{\theta}'), \quad (17)$$

where Q is related to U via

$$Q_{\theta}(\boldsymbol{\theta}) = \frac{2}{\theta^2} \int_0^{\theta} d\boldsymbol{\theta}' \boldsymbol{\theta}' U_{\theta}(\boldsymbol{\theta}') - U_{\theta}(\boldsymbol{\theta}). \quad (18)$$

We also define aperture measures M_{ap} and N_{ap} as functions of projected physical separations \mathbf{r} by

$$M_{\text{ap}}(R; \mathbf{r}) = \int d^2r' U_R(|\mathbf{r} - \mathbf{r}'|) \int d\chi p(\chi) \int d\chi' W(\chi, \chi') \delta(\mathbf{r}', \chi') \quad (19)$$

$$N_{\text{ap}}(R; \mathbf{r}) = \int d^2r' U_R(|\mathbf{r} - \mathbf{r}'|) \int d\chi p(\chi) \delta_{\text{g}}(\mathbf{r}', \chi). \quad (20)$$

Here, R is the aperture scale radius, but in contrast to the θ in Eq. (15), it is in the same physical units, for example Mpc, as r . We also used the relations between three-dimensional densities and projected quantities from Eqs. (4) and (8).

In analogy to M_{ap} , we define an intrinsic alignment aperture measure M_{ap}^I as

$$M_{\text{ap}}^I(\mathbf{R}; \mathbf{r}) = \int d^2 r' U_R(|\mathbf{r} - \mathbf{r}'|) \int d\chi P(\chi) \delta_{\text{I}}(\mathbf{r}', \chi). \quad (21)$$

Throughout, we use the U_θ from Crittenden et al. (2002),

$$U_\theta(\vartheta) = \frac{1}{2\pi\theta} \left(1 - \frac{\vartheta^2}{2\theta^2} \right) \exp\left(-\frac{\vartheta^2}{2\theta^2}\right). \quad (22)$$

For this filter, Schneider & Watts (2005) showed that the correlation function G'_{ggY} can be converted to the third-order aperture statistic through

$$\begin{aligned} & \langle N'_{\text{ap}} N'_{\text{ap}} M'_{\text{ap}} \rangle(\theta_1, \theta_2, \theta_3) \\ &= \langle N'_{\text{ap}}(\theta_1; \boldsymbol{\vartheta}) N'_{\text{ap}}(\theta_2; \boldsymbol{\vartheta}) M'_{\text{ap}}(\theta_3; \boldsymbol{\vartheta}) \rangle \\ &= \int d^2 \vartheta_1 \int d^2 \vartheta_2 G'_{\text{ggY}}(\boldsymbol{\vartheta}_1, \boldsymbol{\vartheta}_2) \mathcal{A}_{\text{NNM}}(\vartheta_1, \vartheta_2, \phi | \theta_1, \theta_2, \theta_3). \end{aligned} \quad (23)$$

where ϕ is the angle between $\boldsymbol{\vartheta}_1$ and $\boldsymbol{\vartheta}_2$ and the kernel function \mathcal{A}_{NNM} is given in the appendix of Schneider & Watts (2005). Similarly, by transforming variables from $\boldsymbol{\vartheta}_i$ to \mathbf{r}_i ,

$$\begin{aligned} & \langle N_{\text{ap}} N_{\text{ap}} M_{\text{ap}}^I \rangle(R_1, R_2, R_3) \\ &= \langle N_{\text{ap}}(\mathbf{R}_1; \mathbf{r}) N_{\text{ap}}(\mathbf{R}_2; \mathbf{r}) M_{\text{ap}}^I(\mathbf{R}_3; \mathbf{r}) \rangle \\ &= \int d^2 r_1 \int d^2 r_2 G_{\text{ggI}}(\mathbf{r}_1, \mathbf{r}_2) \mathcal{A}_{\text{NNM}}(r_1, r_2, \phi | R_1, R_2, R_3), \end{aligned} \quad (24)$$

Our main observable is the aperture statistics $\langle N_{\text{ap}} N_{\text{ap}} M_{\text{ap}}^I \rangle$ for equal aperture radii $R_1 = R_2 = R_3 =: R$. As shown in App. A, $\langle N_{\text{ap}} N_{\text{ap}} M_{\text{ap}}^I \rangle$ can be related to the galaxy-galaxy-shape bispectrum B_{ggI} as

$$\begin{aligned} & \langle N_{\text{ap}} N_{\text{ap}} M_{\text{ap}}^I \rangle(R, R, R) \\ &= \int \frac{d^2 k_{\perp,1}}{(2\pi)^2} \int \frac{d^2 k_{\perp,2}}{(2\pi)^2} \tilde{U}_R(k_{\perp,1}) \tilde{U}_R(k_{\perp,2}) \tilde{U}_R(|k_{\perp,1} + k_{\perp,2}|) \\ & \quad \times \int d\chi P^3(\chi) B_{\text{ggI}}(k_{\perp,1}, k_{\perp,2}, k_{\perp,3}; \chi, \chi, \chi). \end{aligned} \quad (25)$$

2.4. Bispectrum model

We model the bispectrum B_{ggI} motivated by the Non-linear alignment (NLA) IA model (Hirata & Seljak 2004; Bridle & King 2007). According to this model, the power spectrum $P_{\delta\text{I}}$ between matter densities and intrinsic ellipticities is

$$P_{\delta\text{I}}(k) = -A_{\text{IA}} \frac{C_1 \Omega_m \rho_{\text{cr}}}{D(z)} P(k) = f_{\text{IA}} P(k), \quad (26)$$

where P is the non-linear matter power spectrum, Ω_m is the matter density parameter, ρ_{cr} is the critical density, D is the growth factor normalized to unity at the time the alignment is assumed to have occurred, C_1 is a normalization constant and A_{IA} is the intrinsic alignment amplitude. We extend this model to the bispectrum by assuming that the bispectrum $B_{\delta\delta\text{I}}$ between matter densities and the intrinsic ellipticities is

$$B_{\delta\delta\text{I}}(k_1, k_2, k_3; \chi_1, \chi_2, \chi_3) = f_{\text{IA}} B(k_1, k_2, k_3; \chi_1, \chi_2, \chi_3), \quad (27)$$

where B is the matter bispectrum. The bispectrum B_{ggI} between galaxies and the intrinsic ellipticities depends already at leading order on both the linear galaxy bias b and the non-linear galaxy bias b_2 (e.g. Fry & Gaztanaga 1993),

$$B_{\text{ggI}}(k_1, k_2, k_3; \chi_1, \chi_2, \chi_3) = b^2 B_{\delta\delta\text{I}}(k_1, k_2, k_3; \chi_1, \chi_2, \chi_3) \quad (28)$$

$$\begin{aligned} & + \frac{b b_2}{3} [P_{\delta\text{I}}(k_1, \chi_1) P(k_2, \chi_2) + 2 \text{perm.}] \\ &= b^2 f_{\text{IA}} B(k_1, k_2, k_3; \chi_1, \chi_2, \chi_3) \\ & + f_{\text{IA}} \frac{b b_2}{3} [P(k_1, \chi_1) P(k_2, \chi_2) + 2 \text{perm.}]. \end{aligned} \quad (29)$$

This bispectrum contains three free parameters, A_{IA} , b , and b_2 . However, A_{IA} is degenerate with the galaxy bias parameters, as they all determine only the amplitude of the bispectrum. Therefore, we cannot simultaneously constrain the galaxy bias and IA from $\langle N_{\text{ap}} N_{\text{ap}} M_{\text{ap}}^I \rangle$. Instead, we use the value for b estimated by Singh et al. (2015) from second-order statistics. As we argue in Appendix B, we find that for our sample and statistics, the non-linear bias has only a small impact on the model compared to the measurement uncertainty, so we set b_2 to zero and keep only A_{IA} as a free parameter. We model the matter bispectrum B with the *bihalofit* prescription (Takahashi et al. 2020).

3. Measurement

3.1. Correlation function estimator

We measure G^{II_m} for N_L lenses and N_S sources using the estimator

$$\begin{aligned} & \hat{G}_{\text{bias}}^{\text{II}_m}(\mathbf{r}_1, \mathbf{r}_2) \\ &= \frac{\sum_i^{N_L} \sum_j^{N_L} \sum_k^{N_S} \epsilon_k e^{i(\phi_i + \phi_j)} \Delta(r_1, r_2, \phi, \mathbf{x}_i, \mathbf{x}_j, \mathbf{x}_k) \Theta_{\text{II}_m}(\chi_i, \chi_j; \chi_k)}{\sum_i^{N_L} \sum_j^{N_L} \sum_k^{N_S} \Delta(r_1, r_2, \phi, \mathbf{x}_i, \mathbf{x}_j, \mathbf{x}_k) \Theta_{\text{II}_m}(\chi_i, \chi_j; \chi_k)}, \end{aligned} \quad (30)$$

where ϵ_k is the ellipticity of galaxy k , Δ is one if the galaxy positions form a triangle with side lengths r_1 and r_2 and opening angle ϕ and zero otherwise¹, and Θ_{II_m} is one if the lens-source distances are less than or equal to II_m . We evaluate the estimator using an adapted version of the *G3LConGPU*² code presented in Linke et al. (2020b). This code uses GPU acceleration to evaluate the triple sum in Eq. (30) by brute-force. Our changes compared to the version in Linke et al. (2020b) consist of implementing a maximum comoving distance χ_{max} between lenses and sources and using physical instead of angular separations. We measure the correlation function for r_1, r_2 in 20 logarithmic bins between $0.1 h^{-1}$ Mpc and $100 h^{-1}$ Mpc and ϕ in 10 linear bins between 0 and π .

As shown in App. C, this estimator is biased. Its expectation value is

$$\langle \hat{G}_{\text{bias}}^{\text{II}_m} \rangle \simeq \frac{G^{\text{II}_m}}{B(\mathbf{r}_1, \mathbf{r}_2, \text{II}_m)}, \quad (31)$$

¹ In practice, Δ is one, if the side lengths of the galaxy triplet triangle fall into a bin centred on r_1 and r_2 , and thus it depends on the chosen bin width. For ease of notation, we omit this dependency here.

² <https://github.com/llinke1/G3LConGPU>

where

$$\begin{aligned}
 B(\mathbf{r}_1, \mathbf{r}_2, \Pi_m) & \quad (32) \\
 &= \int d\chi \int_{\chi-\Pi_m}^{\chi+\Pi_m} d\chi_1 \int_{\chi-\Pi_m}^{\chi+\Pi_m} d\chi_2 p(\chi_1) p(\chi_2) p(\chi) \\
 & \quad \times [1 + \xi(|\mathbf{r}_1 - \mathbf{r}_2|, |\chi_1 - \chi_2|)],
 \end{aligned}$$

where $\xi(\mathbf{r}, \chi)$ is the three-dimensional two-point correlation function of galaxies with projected separation \mathbf{r} and separation χ along the line of sight. We correct for this bias by multiplying $\hat{G}_{\text{bias}}^{\Pi_m}$ by an estimated B . To obtain this, we estimate the correlation function ξ using a Landy-Szalay estimator as implemented in the code `treecorr` (Jarvis et al. 2004). For the MICE data set, we generate random galaxy positions by uniformly distributing right ascension and declination and drawing redshifts from the redshift distribution of the MICE galaxies. For the LOWZ dataset, we use the same random galaxy sample as Singh & Mandelbaum (2016), provided within BOSS DR12. The $\langle N_{\text{ap}} N_{\text{ap}} M_{\text{ap}}^I \rangle$ is estimated by inserting the unbiased estimator \hat{G}^{Π_m} into Eq. (24).

3.2. Covariance estimate

We estimate the covariance of $\langle N_{\text{ap}} N_{\text{ap}} M_{\text{ap}}^I \rangle$ directly from the data using jackknife resampling, both for the observed LOWZ and simulated MICE galaxies (see Sect. 4). For this, the survey is divided into 100 tiles with approximately the same area. We estimate \hat{G}^{Π_m} for each of these tiles individually. We then combine the estimates for all but the k -th tile to form the k -th jackknife sample and convert it to the aperture statistics, which gives us 100 jackknife samples, we write as $\langle N_{\text{ap}} N_{\text{ap}} M_{\text{ap}}^I \rangle_k$. The i - j component of the covariance of $\langle N_{\text{ap}} N_{\text{ap}} M_{\text{ap}}^I \rangle$ is then

$$\begin{aligned}
 \hat{C}_{ij} &= \frac{100}{100-1} \sum_{k=1}^{100} \left[\langle N_{\text{ap}} N_{\text{ap}} M_{\text{ap}}^I \rangle_k(R_i) - \overline{\langle N_{\text{ap}} N_{\text{ap}} M_{\text{ap}}^I \rangle_k(R_i)} \right] \\
 & \quad \times \left[\langle N_{\text{ap}} N_{\text{ap}} M_{\text{ap}}^I \rangle_k(R_j) - \overline{\langle N_{\text{ap}} N_{\text{ap}} M_{\text{ap}}^I \rangle_k(R_j)} \right], \quad (33)
 \end{aligned}$$

where $\overline{\langle N_{\text{ap}} N_{\text{ap}} M_{\text{ap}}^I \rangle_k(\theta_i)}$ is the average of all aperture statistics jackknife samples. We use $\sigma_i = \sqrt{\hat{C}_{ii}}$ as statistical uncertainty on the measured aperture statistics.

We show the correlation matrix, defined by $\hat{C}_{ij}/(\sigma_i \sigma_j)$, for the LOWZ measurement in Fig. 1. The correlation matrix is dominated by the diagonal, suggesting that shape noise, in contrast to sample variance, is the biggest contributor. However, we see strong non-diagonal contributions. In particular, the signal for nearby scales is strongly correlated. This is expected for aperture statistics. They combine information from the correlation functions at different scales, which causes correlations between the aperture statistics at different aperture radii. The correlation matrix for $\langle N_{\text{ap}} N_{\text{ap}} M_{\text{ap}}^I \rangle$ is qualitatively similar to the correlation matrix for cosmic shear dominated $\langle N_{\text{ap}} N_{\text{ap}} M_{\text{ap}} \rangle$, shown in Fig. 10 of Linke et al. (2022).

3.3. Model fit

We fit the NLA-inspired model defined in Eq. (25) and Eq. (28) to our measurements. This model only includes the galaxy bias

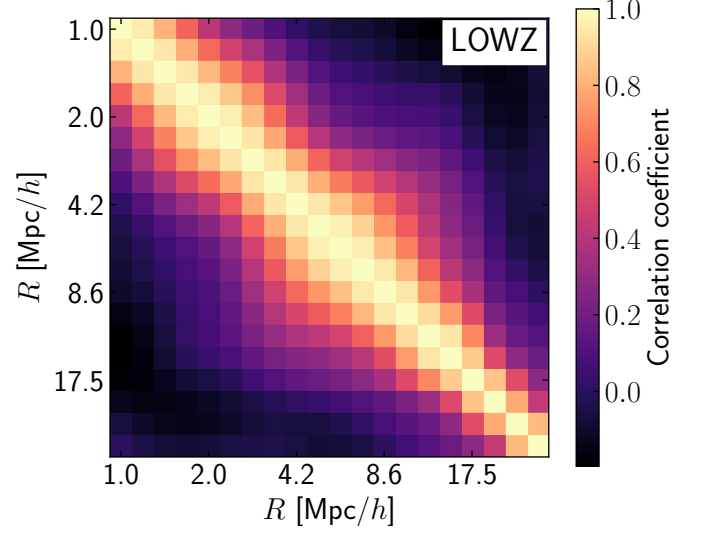


Fig. 1. Correlation matrix estimate from jackknife resampling for the LOWZ measurement, using the full sample as shape tracers.

b and the IA amplitude A_{IA} as free parameters. For the LOWZ galaxies, we use $b = 1.77$ determined by Singh et al. (2015) from second-order statistics. For the MICE galaxies, though, we use $b = 1.47$, which is 17% lower. We use this because the two-point galaxy correlation function in the MICE is approximately 30% lower than in the LOWZ, which suggests this lower galaxy bias value (Hoffmann et al. 2022).

Thus, the only free parameter remaining is A_{IA} , which we obtain by fitting the model to the measurements with a least-squares minimizer (Nelder & Mead 1965), including the covariance matrix obtained in Eq. (33). To investigate the model validity across different scales, we perform two fits for each measurement. One fit considers the aperture statistics for all scales $R \in [1 h^{-1} \text{ Mpc}, 20 h^{-1} \text{ Mpc}]$. This includes much smaller scales than the NLA model is considered valid for second-order statistics. We further conduct a second fit, where we limit the measurements to $R > 6 h^{-1} \text{ Mpc}$. This is the smallest scale considered by Singh et al. (2015) to be valid for the NLA model for second-order statistics. However, we note that the aperture radii R cannot be directly compared to the galaxy separation scale of the two-point correlation function, considered by Singh et al. (2015). Instead, aperture statistics for radius R include the correlation function both at smaller scales and (depending on the filter function) slightly larger scales than R .

4. Data

4.1. SDSS III BOSS LOWZ galaxies

Our primary dataset is the SDSS BOSS LOWZ galaxy sample, previously used by Singh & Mandelbaum (2016). This sample consists of luminous red galaxies (LRGs) at low redshifts, which were observed by DR8 of the SDSS (Aihara et al. 2011) and the BOSS DR11 (Alam et al. 2015). Shape measurements for these galaxies were carried out by Reyes et al. (2012). They reported galaxy ellipticities $\chi = (1 - q^2)/(1 + q^2)$, where q is the minor-to-major axis ratio. However, the ellipticity in Eq. 1 is defined as $\epsilon = (1 - q)/(1 + q)$, so we convert χ to ϵ using the same relation as Singh & Mandelbaum (2016),

$$\epsilon = \frac{\chi}{2\mathcal{R}}, \quad (34)$$

where $\mathcal{R} = 0.925$.

The sample is constructed to contain a volume-limited sample of LRGs, so a selection in both redshift and colour-magnitude space was performed. The selection cuts were

$$\begin{aligned} m_r < 13.5 + c_{\parallel}/0.3 + \Delta m_r & \quad 16.0 < m_r < 19.6 + \Delta m_r, & (35) \\ |c_{\perp}| < 0.2 & \quad 0.16 < z < 0.36, \end{aligned}$$

with

$$\begin{aligned} c_{\parallel} &= 0.7(m_g - m_r) + 1.2[(m_r - m_i) - 0.18] & (36) \\ c_{\perp} &= (m_r - m_i) - 0.25(m_g - m_r) - 0.18. \end{aligned}$$

For the LOWZ galaxies, $\Delta m_r = 0$; however, for the simulated galaxies (see next section), Δm_r needs to be set to 0.085 to match the number density of the observed galaxies. We refer to Singh et al. (2015) for more details on the selection.

Following Singh et al. (2015), we further divide the galaxy sample into four luminosity bins $L_1 - L_4$ with L_1 containing the brightest galaxies. The bins $L_1 - L_3$ each contain 20% of the galaxies, with L_4 containing the remaining 40% faintest galaxies. In the following consider correlations between the shapes of galaxies from one of these luminosity bins with the positions of the whole galaxy sample.

4.2. MICE with IA

To test our measurement pipeline, we use a catalogue of realistically simulated galaxies based on the MICE grand challenge light cone simulation (Fosalba et al. 2015a). MICE is a dark-matter only N -body simulation that adopts a flat Λ CDM cosmology with parameters $\Omega_m = 0.25$, $\Omega_{\Lambda} = 0.75$, $\Omega_b = 0.044$, $n_s = 0.95$, $\sigma_8 = 0.8$, $h = 0.7$. The simulation tracks the evolution of 4096^3 particles, each with a mass of $2.93 \times 10^{10} h^{-1} M_{\odot}$, within a cubic volume of side length $3072 h^{-1}$ Mpc, spanning from an initial redshift of $z = 100$ to the present time. Halos were identified with a Friends-of-friends halo finder (Crocce et al. 2015). Subsequently, the halos were populated with galaxies up to redshift $z = 1.4$, using a combination of halo abundance matching and a halo occupation distribution model (Carretero et al. 2015). The galaxies received positions, luminosities and colours such that their luminosity function and colour-magnitude distribution matched SDSS observations (Blanton et al. 2003; Zehavi et al. 2011).

The MICE was initially designed to accompany gravitational lensing surveys, so an estimate of each galaxy’s weak lensing shear was computed by projecting the mass distribution and applying the Born approximation as described in Fosalba et al. (2015b, 2008). Hoffmann et al. (2022) added realistic intrinsic galaxy ellipticities using a semi-analytic IA model. In this procedure, the simulated galaxies are divided into red and blue central galaxies and satellites; red centrals receive a 3D orientation aligned with their host halo, while blue centrals are aligned with the angular momentum of their host halo. Satellites are assumed to point towards their host halo centre. These orientations are then distorted by a randomly assigned misalignment angle. The distribution of misalignment angles depends on galaxy colour and magnitude. It is calibrated such that the simulated galaxies reproduce the second-order correlation between intrinsic shapes and galaxy positions observed in the LOWZ galaxy sample as well as the observed distribution of galaxy axis ratios from COSMOS (Laigle et al. 2016; Griffith et al. 2012). Simulated galaxy positions, shapes, and other properties for an octant on the sky

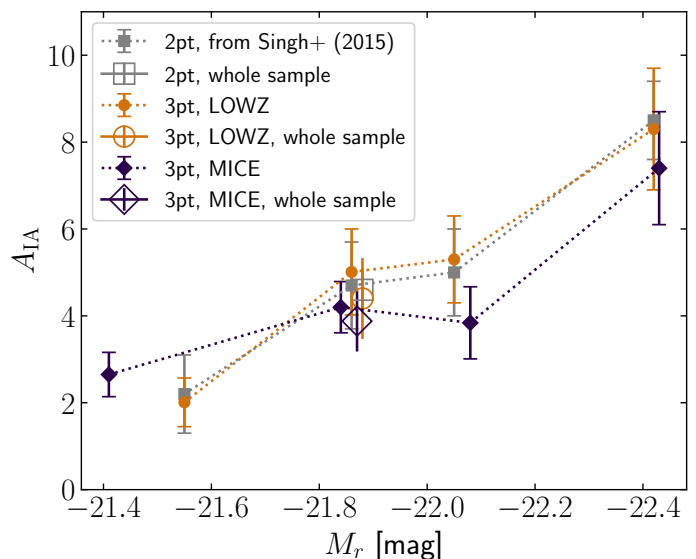


Fig. 2. IA amplitude A_{IA} as a function of the mean absolute magnitude M_r of the shape tracers for the LOWZ galaxies (pink circles) and for the MICE (green diamonds) as obtained from the third-order IA measurement at scales $R > 6 h^{-1}$ Mpc. Also shown are the estimates by Singh et al. (2015) from second-order statistics (black squares). Open symbols are the estimates for the whole shape tracing sample.

are available via Cosmohub³ (Tallada et al. 2020; Carretero et al. 2017)

From the MICE with IA, we select a sample mimicking the LOWZ galaxies on the provided sky octant (5156.6 deg^2 , so approximately half the BOSS footprint). We apply the same selection as in Eq. (35). However, like Hoffmann et al. (2022), we set Δm_r to 0.085 to match the number density of the LOWZ galaxies. As with the LOWZ sample, we divide the simulated galaxies into four luminosity bins, containing 20%, 20%, 20% and 40% of the galaxy sample, respectively. We use only the intrinsic galaxy shapes and neglect the cosmic shear contribution. We also use the ‘true’ (or purely cosmological) redshifts of the sample; that is, we neglect any impact of redshift space distortions.

5. Results

As mentioned in Sect. 3.3, we fit the NLA-inspired model to our measurements firstly using all aperture radii and then restricted to scales above $6 h^{-1}$ Mpc, with galaxy bias values obtained by Singh et al. (2015). The resulting values for A_{IA} are listed in Table 1. In Fig. 2, we show the A_{IA} for the larger-scale fits as a function of the mean absolute magnitude M_r of the samples.

For all luminosity bins, A_{IA} is significantly non-zero. Using the large-scale (all-scale) fit, A_{IA} for the full LOWZ sample is 4.7σ (7.6σ) larger than zero. The strongest detection occurs for the brightest sample with 5.9σ for the large-scale fit. As expected, A_{IA} is largest for the brightest galaxies, which are expected to show the strongest alignment, and decreases for fainter galaxies.

Also shown in Fig. 2, and listed in Table 1, are the values for A_{IA} estimated by Singh et al. (2015) from second-order correlations. Our third-order based estimates are consistent with these second-order based estimates within their 1σ uncertainties for all luminosity bins.

³ www.cosmohub.pic.es

Table 1. Intrinsic alignment amplitudes from model fits to LOWZ and MICE galaxies

	LOWZ						MICE			
	A_{IA} (2pt)	$\langle M_r \rangle$	$\langle z \rangle$	A_{IA} (3pt, large scales)	A_{IA} (3pt, all)		$\langle M_r \rangle$	$\langle z \rangle$	A_{IA} (3pt, large scales)	A_{IA} (3pt, all)
all	4.6 ± 0.5	-21.88	0.28	4.40 ± 0.93	3.99 ± 0.53		-21.84	0.26	4.20 ± 0.59	3.90 ± 0.56
L1	8.5 ± 0.9	-22.42	0.28	8.3 ± 1.4	7.02 ± 0.76		-22.43	0.29	7.4 ± 1.3	6.65 ± 0.72
L2	5.0 ± 1.0	-22.05	0.28	5.3 ± 1.0	4.57 ± 0.58		-22.08	0.28	3.84 ± 0.83	4.39 ± 0.48
L3	4.7 ± 1.0	-21.86	0.28	5.01 ± 0.99	3.58 ± 0.45		-21.87	0.27	3.88 ± 0.70	4.77 ± 0.46
L4	2.2 ± 0.9	-21.55	0.28	2.01 ± 0.56	1.88 ± 0.31		-21.41	0.24	3.05 ± 0.51	2.33 ± 0.31

Notes. The A_{IA} were obtained by Singh et al. (2015) from second-order statistics (second column), the third-order measurements at $R > 6 h^{-1}$ Mpc (fifth and ninth column), and at all scales (sixth and tenth column). Also shown are the average absolute magnitude $\langle M_r \rangle$ and the average redshift $\langle z \rangle$ of the samples. Bold denotes values that differ more than 1σ from the second-order estimates.

Figure 2 also shows the A_{IA} obtained from fitting the model to the measurements for the simulated MICE galaxies. Their A_{IA} show the same trends as for the observed galaxies and agree with them within $1-2\sigma$. Generally, A_{IA} is lower in the simulation than observed, except for the faintest galaxies in the L4 sample. However, the MICE galaxies have slightly different mean luminosities and luminosity distributions, so slight differences are not unexpected.

Table 1 shows that we obtain smaller values for A_{IA} when fitting to all measured scales than when considering only larger scales. To understand this, we show the measurement and both fits for the full sample in Fig. 3 and the individual luminosity bins in Fig. 4. For all LOWZ galaxy samples the signal flattens at small scales. This flattening cannot be described by our simple model that only contains a scale-independent parameter. The fit compensates for this inadequacy by lowering A_{IA} across all scales.

Even when including the small scales, the model provides a reasonable fit to the data, with the model deviating nowhere at more than 1σ from the measurements. However, the difference between the inferred A_{IA} and the estimate from second-order statistics is greater. For the L1 and L3 galaxies, the estimates no longer agree within the 1σ uncertainty, so the extrapolation of the third-order model to small scales is not consistent with the second-order model at larger scales.

The MICE galaxies show the same trends as the LOWZ galaxies. Aside from the L2 sample, we see the same flattening of the signal at small scales. For the brightest galaxies, we also find a more than 1σ difference in the A_{IA} inferred from the fit to the whole scale range compared to the second-order estimate.

6. Discussion

We presented the first detection of a third-order intrinsic alignment (IA) correlation in the SDSS BOSS LOWZ galaxies. For this, we measured the third-order correlation function between galaxy positions and shapes and expressed them in terms of aperture statistics. We compared the measured signal with predictions by the MICE cosmological simulation and a non-linear alignment (NLA) based analytical model. Our measurements depend on the $B_{\delta\delta 1}$ contribution to the bispectrum of matter densities and galaxy shapes, the matter-matter-shape correlation. The positions of the LOWZ galaxies are used as tracers for the matter distribution, which were then correlated with their shapes.

We find a significant third-order IA signal. For scales between $6 h^{-1}$ Mpc and $20 h^{-1}$ Mpc and using the full LOWZ galaxy sample, we find an IA amplitude $A_{IA} = 4.4 \pm 0.93$, which is a non-zero signal at 4.7σ . After dividing the sample into subsamples based on galaxy luminosity, we find an increased S/N

for the brightest galaxies while the S/N for the fainter galaxies decreases. However, even for the faintest galaxies, A_{IA} is still non-zero at 3.6σ . This dependence of the signal on the galaxy luminosity is not surprising, as IA has been shown to increase with galaxy luminosity / stellar mass, both in observations (Singh et al. 2015; Singh & Mandelbaum 2016; Johnston et al. 2019) and hydrodynamical simulations (Samuroff et al. 2021).

Comparing the measurements from the observations to the predictions by the MICE simulation, we again find that the best-fitting A_{IA} increases with luminosity. Indeed the A_{IA} from the simulation agree with the LOWZ measurements at $1-2\sigma$. At first glance, this agreement might seem unsurprising as the intrinsic shapes of the simulated galaxies have been tuned to reproduce the second-order IA measurements by Singh et al. (2015) in the LOWZ sample. Moreover, the third-order galaxy clustering of MICE galaxies has been successfully validated (Hoffmann et al. 2015). However, the agreement is a crucial consistency check for two reasons. First, the agreement suggests that tuning the simulation to the second-order statistics automatically provides the correct third-order statistics, lending credibility to the physical model implemented in the simulation. Second, only the intrinsic galaxy shapes were used for the simulation measurements without adding cosmic shear. Consequently, the agreement of the measurements in the observations, where we cannot turn off cosmic shear, shows that weak lensing does not significantly bias our measurement. This validates our choice of Π_m , the maximal distance between galaxies in a triplet considered for the correlation function measurement. Evidently, the chosen Π_m is small enough that cosmic shear correlations become sub-dominant.

Finally, we compared the A_{IA} from the model fits to the third-order IA signal to the estimates by Singh et al. (2015) from second-order statistics. The A_{IA} obtained from fitting to scales above $6 h^{-1}$ Mpc agree within 1σ with the second-order estimates. Consequently, at these scales, the second- and third-order models are consistent and can be used in a combined analysis. This combination offers the opportunity for IA self-calibration (Pyne & Joachimi 2021), leading to tighter constraints on both IA and cosmological parameters.

The A_{IA} values inferred from the fit including smaller scales agree less well with the second-order based estimates. While the agreement is still within 2σ for all luminosity samples, the measurements show a flattening at small scales that cannot be described with our simple NLA-inspired model. This is a hint that the model is no longer accurate at small scales - an unsurprising finding, as Singh et al. (2015) already found that the NLA model cannot well describe the second-order IA statistics for scales below $6 h^{-1}$ Mpc. As mentioned before, the NLA model is an effective, phenomenological description of IA and not rigorously physically motivated. Thus, inaccuracies, in particular at small scales, are to be expected.

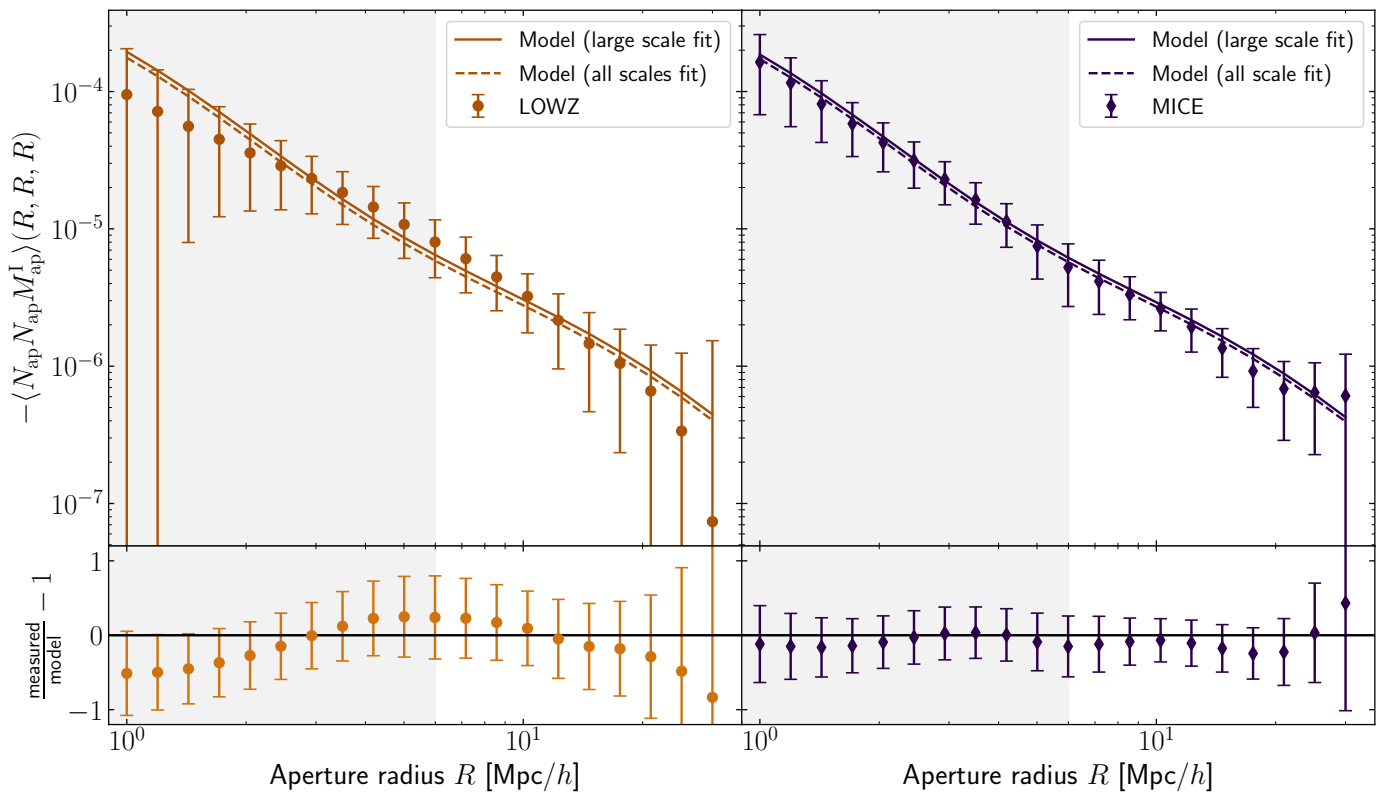


Fig. 3. Upper panels: Intrinsic alignment aperture statistics for full galaxy samples. The left panel shows the measurements for the LOWZ galaxies; right panel shows measurements for the simulated MICE galaxies. Points are measurements with jackknife error estimates. Solid lines show the model fit using scales above $6 h^{-1}$ Mpc; dashed lines are the model fit using all shown scales. Lower panels: Relative difference of measurement to model fit for large scales.

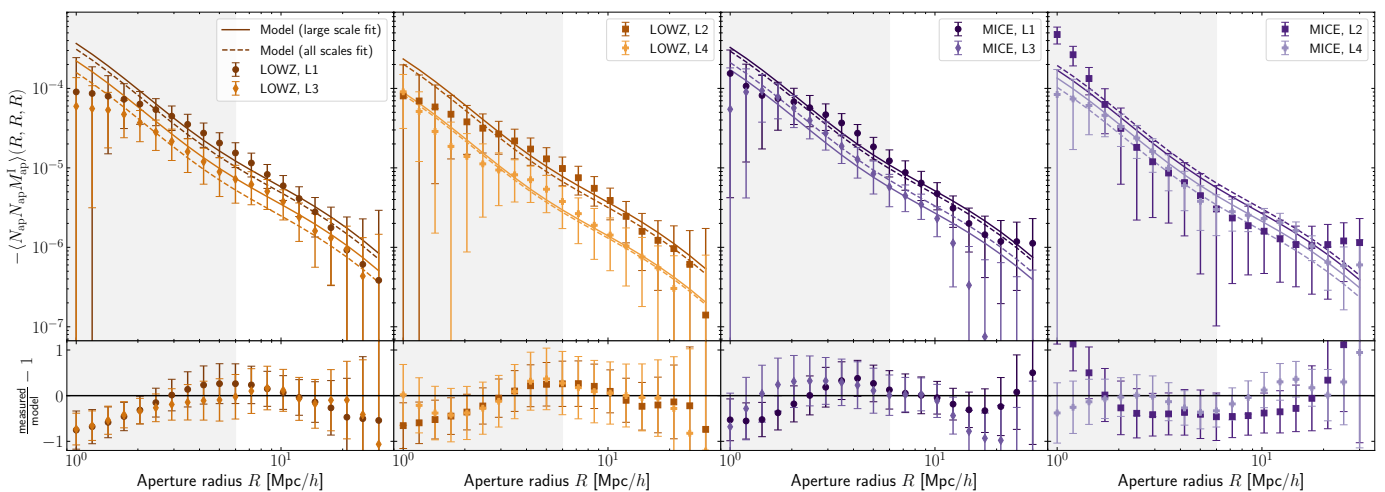


Fig. 4. Same as Fig. 3, but for the different luminosity samples, with L1 containing the brightest and L4 the faintest galaxies.

Another consideration in explaining the model deviations aside from the inaccuracies of the NLA model is our choice of a simple linear deterministic galaxy bias. In a perturbation theory approach, the galaxy bispectrum already depends on the non-linear galaxy bias at the leading order. We showed that a non-zero non-linear bias only has a small impact on the model compared to the measurement uncertainties and thus can be neglected.

The perturbation theory approach itself becomes inaccurate when entering the regime of single dark matter halos, so a more sophisticated third-order IA model might be needed at small

scales. For example, the bispectrum B_{ggI} could be modelled by using a halo model approach for the correlation between galaxies and matter (Linke et al. 2022), multiplied by the NLA prefactor f_1 . Alternatively, a full halo model for the IA signal might be devised in the spirit of Fortuna et al. (2021). However, in light of the general good agreement, we see no necessity to use a more complex IA model to describe the LOWZ data set. This might change for other surveys with more constraining power, for example those expected by *Euclid*, LSST, and DESI. Repeating our measurements on a more extensive survey and other galaxy samples will help decide whether the NLA-inspired model is still ap-

appropriate for analysing third-order statistics in upcoming stage-IV surveys. Additionally, other third-order statistics, for example, shape-shape-lens correlations or the related bispectra, could be explored to further test the model consistency.

Acknowledgements. The authors acknowledge the support of the Lorentz Center and the echoIA project. LL is supported by the Austrian Science Fund (FWF) [ESP 357-N]. SP and BJ acknowledge support by the ERC-selected UKRI Frontier Research Grant EP/Y03015X/1. This publication is part of the project “A rising tide: Galaxy intrinsic alignments as a new probe of cosmology and galaxy evolution” (with project number VI.Vidi.203.011) of the Talent programme Vidi which is (partly) financed by the Dutch Research Council (NWO). RM acknowledges the support of the Simons Foundation (Simons Investigator in Astrophysics, Award ID 620789). This work has made use of CosmoHub. CosmoHub has been developed by the Port d’Informació Científica (PIC), maintained through a collaboration of the Institut de Física d’Altes Energies (IFAE) and the Centro de Investigaciones Energéticas Medioambientales y Tecnológicas (CIEMAT) and the Institute of Space Sciences (CSIC & IEEC). CosmoHub was partially funded by the “Plan Estatal de Investigación Científica y Técnica de Innovación” program of the Spanish government, has been supported by the call for grants for Scientific and Technical Equipment 2021 of the State Program for Knowledge Generation and Scientific and Technological Strengthening of the R+D+i System, financed by MCIN/AEI/ 10.13039/501100011033 and the EU NextGeneration/PRTR (Hadoop Cluster for the comprehensive management of massive scientific data, reference EQC2021-007479-P) and by MICIIN with funding from European Union NextGenerationEU(PRTR-C17.I1) and by Generalitat de Catalunya. Funding for SDSS-III has been provided by the Alfred P. Sloan Foundation, the Participating Institutions, the National Science Foundation, and the U.S. Department of Energy Office of Science. The SDSS-III website is <http://www.sdss3.org/>. SDSS-III is managed by the Astrophysical Research Consortium for the Participating Institutions of the SDSS-III Collaboration including the University of Arizona, the Brazilian Participation Group, Brookhaven National Laboratory, Carnegie Mellon University, University of Florida, the French Participation Group, the German Participation Group, Harvard University, the Instituto de Astrofísica de Canarias, the Michigan State/Notre Dame/JINA Participation Group, Johns Hopkins University, Lawrence Berkeley National Laboratory, Max Planck Institute for Astrophysics, Max Planck Institute for Extraterrestrial Physics, New Mexico State University, New York University, Ohio State University, Pennsylvania State University, University of Portsmouth, Princeton University, the Spanish Participation Group, University of Tokyo, University of Utah, Vanderbilt University, University of Virginia, University of Washington, and Yale University.

References

- Abbott, T., Abdalla, F. B., Allam, S., et al. 2016, *Phys. Rev. D*, 94, 022001
- Aihara, H., Allende Prieto, C., An, D., et al. 2011, *ApJS*, 193, 29
- Aihara, H., Arimoto, N., Armstrong, R., et al. 2018, *PASJ*, 70, S4
- Akeson, R., Armus, L., Bachelet, E., et al. 2019, arXiv e-prints, arXiv:1902.05569
- Alam, S., Albareti, F. D., Allende Prieto, C., et al. 2015, *ApJS*, 219, 12
- Amon, A., Gruen, D., Troxel, M. A., et al. 2022, *Phys. Rev. D*, 105, 023514
- Asgari, M., Lin, C.-A., Joachimi, B., et al. 2021, *A&A*, 645, A104
- Bartelmann, M. & Schneider, P. 2001, *Phys. Rep.*, 340, 291
- Becker, M. R., Troxel, M. A., MacCrann, N., et al. 2016, *Phys. Rev. D*, 94, 022002
- Blanton, M. R., Hogg, D. W., Bahcall, N. A., et al. 2003, *ApJ*, 592, 819
- Blazek, J. A., MacCrann, N., Troxel, M. A., & Fang, X. 2019, *Phys. Rev. D*, 100, 103506
- Bridle, S. & King, L. 2007, *New Journal of Physics*, 9, 444
- Burger, P. A., Porth, L., Heydenreich, S., et al. 2024, *A&A*, 683, A103
- Carretero, J., Castander, F. J., Gaztañaga, E., Crocce, M., & Fosalba, P. 2015, *MNRAS*, 447, 646
- Carretero, J., Tallada, P., Casals, J., et al. 2017, in *Proceedings of the European Physical Society Conference on High Energy Physics*. 5-12 July, 488
- Catelan, P., Kamionkowski, M., & Blandford, R. D. 2001, *MNRAS*, 320, L7
- Chen, S.-F. & Kokron, N. 2024, *J. Cosmology Astropart. Phys.*, 1, 027
- Crittenden, R. G., Natarajan, P., Pen, U.-L., & Theuns, T. 2002, *ApJ*, 568, 20
- Crocce, M., Castander, F. J., Gaztañaga, E., Fosalba, P., & Carretero, J. 2015, *MNRAS*, 453, 1513
- Dalal, R., Li, X., Nicola, A., et al. 2023, *Phys. Rev. D*, 108, 123519
- DES and KiDS Collaboration: Abbott, T. M. C., Aguena, M., Alarcon, A., et al. 2023, *The Open Journal of Astrophysics*, 6, 36
- Eggemeier, A., Scoccimarro, R., Smith, R. E., et al. 2021, *Phys. Rev. D*, 103, 123550
- Euclid Collaboration: Ajani, V., Baldi, M., Barthelemy, A., et al. 2023, *A&A*, 675, A120
- Euclid Collaboration: Mellier, Y., Abdurro’uf, Acevedo Barroso, J., Achúcarro, A., et al. 2024, *A&A*, submitted, arXiv:2405.13491
- Fortuna, M. C., Hoekstra, H., Johnston, H., et al. 2021, *A&A*, 654, A76
- Fosalba, P., Crocce, M., Gaztañaga, E., & Castander, F. J. 2015a, *MNRAS*, 448, 2987
- Fosalba, P., Gaztañaga, E., Castander, F. J., & Crocce, M. 2015b, *MNRAS*, 447, 1319
- Fosalba, P., Gaztañaga, E., Castander, F. J., & Manera, M. 2008, *MNRAS*, 391, 435
- Fry, J. N. & Gaztanaga, E. 1993, *ApJ*, 413, 447
- Gil-Marín, H., Percival, W. J., Verde, L., et al. 2017, *MNRAS*, 465, 1757
- Griffith, R. L., Cooper, M. C., Newman, J. A., et al. 2012, *ApJS*, 200, 9
- Hirata, C. M., Mandelbaum, R., Ishak, M., et al. 2007, *MNRAS*, 381, 1197
- Hirata, C. M. & Seljak, U. 2004, *Phys. Rev. D*, 70, 063526
- Hoffmann, K., Bel, J., Gaztañaga, E., et al. 2015, *MNRAS*, 447, 1724
- Hoffmann, K., Secco, L. F., Blazek, J., et al. 2022, *Phys. Rev. D*, 106, 123510
- Ivezić, Ž., Kahn, S. M., Tyson, J. A., et al. 2019, *ApJ*, 873, 111
- Jarvis, M., Bernstein, G., & Jain, B. 2004, *MNRAS*, 352, 338
- Joachimi, B., Cacciato, M., Kitching, T. D., et al. 2015, *Space Sci. Rev.*, 193, 1
- Joachimi, B., Mandelbaum, R., Abdalla, F. B., & Bridle, S. L. 2011, *A&A*, 527, A26
- Johnston, H., Georgiou, C., Joachimi, B., et al. 2019, *A&A*, 624, A30
- Johnston, H., Joachimi, B., Norberg, P., et al. 2021, *A&A*, 646, A147
- Kaiser, N. & Squires, G. 1993, *ApJ*, 404, 441
- Kiessling, A., Cacciato, M., Joachimi, B., et al. 2015, *Space Sci. Rev.*, 193, 67
- Kirk, D., Brown, M. L., Hoekstra, H., et al. 2015, *Space Sci. Rev.*, 193, 139
- Kuijken, K., Heymans, C., Hildebrandt, H., et al. 2015, *MNRAS*, 454, 3500
- Laigle, C., McCracken, H. J., Ilbert, O., et al. 2016, *ApJS*, 224, 24
- Lamman, C., Tsaprazi, E., Shi, J., et al. 2024, *The Open Journal of Astrophysics*, 7, 14
- Laureijs, R., Amiaux, J., Arduini, S., et al. 2011, arXiv e-prints, arXiv:1110.3193
- Li, X., Zhang, T., Sugiyama, S., et al. 2023, *Phys. Rev. D*, 108, 123518
- Linke, L., Simon, P., Schneider, P., et al. 2020a, *A&A*, 640, A59
- Kirk, D., Brown, M. L., Hoekstra, H., et al. 2015, *Space Sci. Rev.*, 193, 139
- Linke, L., Simon, P., Schneider, P., et al. 2022, *A&A*, 665, A38
- Linke, L., Simon, P., Schneider, P., & Hilbert, S. 2020b, *A&A*, 634, A13
- Maion, F., Angulo, R. E., Bakx, T., et al. 2023, arXiv e-prints, arXiv:2307.13754
- Nelder, J. A. & Mead, R. 1965, *The Computer Journal*, 7, 308
- Pyne, S. & Joachimi, B. 2021, *MNRAS*, 503, 2300
- Pyne, S., Tenneti, A., & Joachimi, B. 2022, *MNRAS*, 516, 1829
- Reyes, R., Mandelbaum, R., Gunn, J. E., et al. 2012, *MNRAS*, 425, 2610
- Samuroff, S., Mandelbaum, R., & Blazek, J. 2021, *MNRAS*, 508, 637
- Samuroff, S., Mandelbaum, R., Blazek, J., et al. 2023, *MNRAS*, 524, 2195
- Schneider, M. D. & Bridle, S. 2010, *MNRAS*, 402, 2127
- Schneider, P. & Lombardi, M. 2003, *A&A*, 397, 809
- Schneider, P., van Waerbeke, L., Kilbinger, M., & Mellier, Y. 2002, *A&A*, 396, 1
- Schneider, P. & Watts, P. 2005, *A&A*, 432, 783
- Semboloni, E., Heymans, C., van Waerbeke, L., & Schneider, P. 2008, *MNRAS*, 388, 991
- Simon, P., Schneider, P., & Kübler, D. 2012, *A&A*, 548, A102
- Singh, S. & Mandelbaum, R. 2016, *MNRAS*, 457, 2301
- Singh, S., Mandelbaum, R., & More, S. 2015, *MNRAS*, 450, 2195
- Takahashi, R., Nishimichi, T., Namikawa, T., et al. 2020, *ApJ*, 895, 113
- Takahashi, R., Sato, M., Nishimichi, T., Taruya, A., & Oguri, M. 2012, *ApJ*, 761, 152
- Tallada, P., Carretero, J., Casals, J., et al. 2020, *Astronomy and Computing*, 32, 100391
- Troxel, M. A. & Ishak, M. 2015, *Phys. Rep.*, 558, 1
- Vlah, Z., Chisari, N. E., & Schmidt, F. 2020, *J. Cosmology Astropart. Phys.*, 01, 025
- Zehavi, I., Zheng, Z., Weinberg, D. H., et al. 2011, *ApJ*, 736, 59

Appendix A: Relation of aperture statistics to bispectrum

To model $\langle N_{\text{ap}} N_{\text{ap}} M_{\text{ap}}^I \rangle$, we relate it to the galaxy-galaxy-shape bispectrum B_{ggI} . For this, we first write it as

$$\begin{aligned} \langle N_{\text{ap}} N_{\text{ap}} M_{\text{ap}}^I \rangle (R_1, R_2, R_3) &= \int d\chi p(\chi) \int d\chi_1 p(\chi_1) \int d\chi_2 p(\chi_2) \int d^2 r'_1 \int d^2 r'_2 \int d^2 r'_3 U_R(r'_1) U_R(r'_2) U_R(r'_3) \\ &\quad \times \langle \delta_{\text{g}}(\mathbf{r} - \mathbf{r}_1, \chi_1) \delta_{\text{g}}(\mathbf{r} - \mathbf{r}_2, \chi_2) \delta_1(\mathbf{r} - \mathbf{r}_3, \chi) \rangle . \end{aligned} \quad (\text{A.1})$$

We now use the galaxy-galaxy-intrinsic shape bispectrum B_{ggI} defined by

$$(2\pi)^3 \delta_{\text{D}}(\mathbf{k}_1 + \mathbf{k}_2 + \mathbf{k}_3) B_{\text{ggI}}(k_1, k_2, k_3; \chi_1, \chi_2, \chi) = \langle \tilde{\delta}_{\text{g}}(\mathbf{k}_1, \chi_1) \tilde{\delta}_{\text{g}}(\mathbf{k}_2, \chi_2) \tilde{\delta}_1(\mathbf{k}_3, \chi) \rangle , \quad (\text{A.2})$$

and separate the \mathbf{k}_i into their components $k_{z,i}$ along the line-of-sight and $\mathbf{k}_{\perp,i}$ perpendicular to the line-of-sight. With this,

$$\begin{aligned} \langle N_{\text{ap}} N_{\text{ap}} M_{\text{ap}}^I \rangle (R_1, R_2, R_3) &= \int d\chi p(\chi) \int d\chi_1 p(\chi_1) \int d\chi_2 p(\chi_2) \int \frac{d^2 k_{\perp,1}}{(2\pi)^2} \int \frac{d^2 k_{\perp,2}}{(2\pi)^2} \int \frac{d^2 k_{\perp,3}}{(2\pi)^2} \tilde{U}_R(k_{\perp,1}) \tilde{U}_R(k_{\perp,2}) \tilde{U}_R(k_{\perp,3}) \\ &\quad \times \int \frac{dk_{z,1}}{2\pi} \int \frac{dk_{z,2}}{2\pi} \int \frac{dk_{z,3}}{2\pi} e^{-i(k_{z,1}\chi_1 + k_{z,2}\chi_2 + k_{z,3}\chi)} (2\pi)^3 \delta_{\text{D}}(\mathbf{k}_1 + \mathbf{k}_2 + \mathbf{k}_3) B_{\text{ggI}}(k_1, k_2, k_3; \chi_1, \chi_2, \chi) . \end{aligned} \quad (\text{A.3})$$

Evaluating the k_3 integrals leads to

$$\begin{aligned} \langle N_{\text{ap}} N_{\text{ap}} M_{\text{ap}}^I \rangle (R_1, R_2, R_3) &= \int d\chi p(\chi) \int d\chi_1 p(\chi_1) \int d\chi_2 p(\chi_2) \int \frac{d^2 k_{\perp,1}}{(2\pi)^2} \int \frac{d^2 k_{\perp,2}}{(2\pi)^2} \tilde{U}_R(k_{\perp,1}) \tilde{U}_R(k_{\perp,2}) \tilde{U}_R(|k_{\perp,1} + k_{\perp,2}|) \\ &\quad \times \int \frac{dk_{z,1}}{2\pi} \int \frac{dk_{z,2}}{2\pi} e^{-ik_{z,1}(\chi_1 - \chi) + ik_{z,2}(\chi_2 - \chi)} B_{\text{ggI}}(k_1, k_2, k_3; \chi_1, \chi_2, \chi) . \end{aligned} \quad (\text{A.4})$$

Now, we use the Limber approximation, under which

$$B_{\text{ggI}}(k_1, k_2, k_3; \chi_1, \chi_2, \chi) \simeq B_{\text{ggI}}(k_{\perp,1}, k_{\perp,2}, k_{\perp,3}; \chi_1, \chi_2, \chi) . \quad (\text{A.5})$$

Inserting this, evaluating the $k_{z,i}$ integrals and the (then trivial) χ_1 and χ_2 integrals leads to

$$\langle N_{\text{ap}} N_{\text{ap}} M_{\text{ap}}^I \rangle (R_1, R_2, R_3) = \int \frac{d^2 k_{\perp,1}}{(2\pi)^2} \int \frac{d^2 k_{\perp,2}}{(2\pi)^2} \tilde{U}_R(k_{\perp,1}) \tilde{U}_R(k_{\perp,2}) \tilde{U}_R(|k_{\perp,1} + k_{\perp,2}|) \int d\chi p^3(\chi) B_{\text{ggI}}(k_{\perp,1}, k_{\perp,2}, k_{\perp,3}; \chi, \chi, \chi) , \quad (\text{A.6})$$

so $\langle N_{\text{ap}} N_{\text{ap}} M_{\text{ap}}^I \rangle$ can be readily computed for a given filter function U , a galaxy redshift distribution p and a bispectrum model B_{ggI} .

Appendix B: Impact of non-linear galaxy bias

As described in Eq. (28), the galaxy-matter bispectrum already depends on the non-linear galaxy bias b_2 at the leading order. However, we argue that b_2 can be neglected for the $\langle N_{\text{ap}} N_{\text{ap}} M_{\text{ap}}^I \rangle$ modelling at the level of uncertainty of the LOWZ measurements. To demonstrate this, Fig. B.1 shows the best-fitting model for the LOWZ measurements in the full sample when neglecting b_2 and the model for the same A_{IA} and b but now setting $b_2 = 1$. For this, we computed the non-linear power spectrum using the revised `halofit` prescription (Takahashi et al. 2012).

When including a positive b_2 , the model increases, particularly at larger scales, by up to 20%. However, this increase is small compared to the measurement uncertainty and both models show good agreement with the measurement. Therefore, the value of b_2 is not critical to describe the $\langle N_{\text{ap}} N_{\text{ap}} M_{\text{ap}}^I \rangle$ from the LOWZ.

We note that Fig B.1 depicts a pessimistic case, as we do not expect b_2 to be as large as one. Measurements of the bispectrum of galaxies from the LOWZ sample by Gil-Marín et al. (2017) found $b_2 \sigma_8 = 0.6$, which for $\sigma_8 = 0.8$ yields $b_2 = 0.75$. Using LOWZ-like simulated mock galaxies, Eggemeier et al. (2021) found the even lower value of $b_2 = 0.3 \pm 0.2$. Consequently, the impact of the non-linear galaxy bias is likely even smaller than shown here.

Appendix C: Estimator bias

The estimator for the correlation function in Eq. (30) is biased. To see this, we calculate the expectation value of the estimator. The expectation value of the numerator is

$$\left\langle \sum_{i=1}^{N_L} \sum_{j=1}^{N_L} \sum_{k=1}^{N_S} \epsilon_k e^{i(\phi_i + \phi_j)} \Delta(r_1, r_2, \phi, \mathbf{x}_i, \mathbf{x}_j, \mathbf{x}_k) \Theta_{\Pi_m}(\chi_i, \chi_j; \chi_k) \right\rangle \quad (\text{C.1})$$

$$\begin{aligned} &= \int d^2 x_1 \int d^2 x_2 \int d^2 x_3 \int d\chi_1 \int d\chi_2 \int d\chi_3 p(\chi_1) p(\chi_2) p(\chi_3) \langle n(\mathbf{x}_1, \chi_1) n(\mathbf{x}_2, \chi_2) \epsilon(\mathbf{x}_3, \chi_3) e^{-i(\phi_1 + \phi_2)} \rangle \\ &\quad \times \Delta(r_1, r_2, \phi, \mathbf{x}_1, \mathbf{x}_2, \mathbf{x}_3) \Theta_{\Pi_m}(\chi_1, \chi_2; \chi_3) \end{aligned} \quad (\text{C.2})$$

$$\begin{aligned} &= \int d\chi \int_{\chi - \Pi_m}^{\chi + \Pi_m} d\chi_1 \int_{\chi - \Pi_m}^{\chi + \Pi_m} d\chi_2 p(\chi_1) p(\chi_2) p(\chi) \langle n(\mathbf{x}_3 + \mathbf{r}_1, \chi_1) n(\mathbf{x}_3 + \mathbf{r}_2, \chi_2) \epsilon(\mathbf{x}_3, \chi) e^{-i(\phi_1 + \phi_2)} \rangle \\ &= \bar{N}_{\Pi_m}^2 G^{\Pi_m}(\mathbf{r}_1, \mathbf{r}_2) . \end{aligned} \quad (\text{C.3})$$

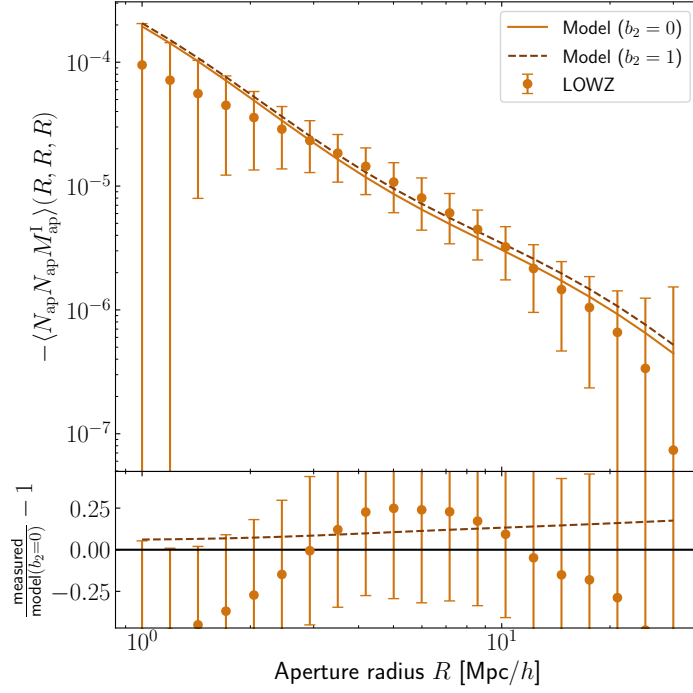


Fig. B.1. Upper panel: Measurement of $\langle N_{\text{ap}} N_{\text{ap}} M_{\text{ap}}^1 \rangle$ for full LOWZ sample (points), with model fit without non-linear bias (solid line) and same model but using $b_2 = 1$ (dashed line). Lower panel: Relative difference to the model which neglects non-linear bias.

The expectation value of the denominator is

$$\left\langle \sum_{i=1}^{N_L} \sum_{j=1}^{N_L} \sum_{k=1}^{N_S} \Delta(r_1, r_2, \phi, \mathbf{x}_i, \mathbf{x}_j, \mathbf{x}_k) \Theta_{\Pi_m}(\chi_i, \chi_j; \chi_k) \right\rangle \quad (\text{C.4})$$

$$= \int d^2 x_1 \int d^2 x_2 \int d^2 x_3 \int d\chi_1 \int d\chi_2 \int d\chi_3 p(\chi_1) p(\chi_2) p(\chi_3) \langle n(\mathbf{x}_1, \chi_1) n(\mathbf{x}_2, \chi_2) \rangle \Delta(r_1, r_2, \phi, \mathbf{x}_1, \mathbf{x}_2, \mathbf{x}_3) \Theta_{\Pi_m}(\chi_1, \chi_2, \chi_3) \quad (\text{C.5})$$

$$= \int d\chi \int_{\chi - \Pi_m}^{\chi + \Pi_m} d\chi_1 \int_{\chi - \Pi_m}^{\chi + \Pi_m} d\chi_2 p(\chi_1) p(\chi_2) p(\chi) \langle n(\mathbf{x}_3 + \mathbf{r}_1, \chi_1) n(\mathbf{x}_3 + \mathbf{r}_2, \chi_2) \rangle \quad (\text{C.6})$$

$$= \int d\chi \int_{\chi - \Pi_m}^{\chi + \Pi_m} d\chi_1 \int_{\chi - \Pi_m}^{\chi + \Pi_m} d\chi_2 p(\chi_1) p(\chi_2) p(\chi) \times \bar{n}(\chi_1) \bar{n}(\chi_2) [1 + \xi(|\mathbf{r}_1 - \mathbf{r}_2|, |\chi_1 - \chi_2|)]. \quad (\text{C.7})$$

Here, $\xi(\Delta r, \Delta \chi)$ is the three-dimensional galaxy clustering function for galaxy pairs separated by Δr in projection and by $\Delta \chi$ along the line-of-sight. This expectation value can be approximated by

$$\int d\chi \int_{\chi - \Pi_m}^{\chi + \Pi_m} d\chi_1 \int_{\chi - \Pi_m}^{\chi + \Pi_m} d\chi_2 p(\chi_1) p(\chi_2) p(\chi) \bar{n}(\chi_1) \bar{n}(\chi_2) [1 + \xi(|\mathbf{r}_1 - \mathbf{r}_2|, |\chi_1 - \chi_2|)] \quad (\text{C.8})$$

$$\simeq \bar{N}_{\Pi_m}^2 \int d\chi \int_{\chi - \Pi_m}^{\chi + \Pi_m} d\chi_1 \int_{\chi - \Pi_m}^{\chi + \Pi_m} d\chi_2 p(\chi_1) p(\chi_2) p(\chi) [1 + \xi(|\mathbf{r}_1 - \mathbf{r}_2|, |\chi_1 - \chi_2|)]$$

$$= \bar{N}_{\Pi_m}^2 B(\mathbf{r}_1, \mathbf{r}_2, \Pi_m).$$

Therefore, the expectation value of the estimator $\hat{G}_{\text{bias}}^{\Pi_m}$ is

$$\langle \hat{G}_{\text{bias}}^{\Pi_m} \rangle \simeq \frac{G^{\Pi_m}}{B(\mathbf{r}_1, \mathbf{r}_2, \Pi_m)}. \quad (\text{C.9})$$